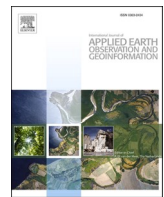




Contents lists available at ScienceDirect

International Journal of Applied Earth Observations and Geoinformation

journal homepage: www.elsevier.com/locate/jag

Surge of Mangla reservoir loading promoted failure on active Décollement of western Himalayas

Lei Xie^a, Wenbin Xu^{b,*}, Xiaoge Liu^b, Xiaoli Ding^a^a The Department of Land Surveying and Geo-Informatics, The Hong Kong Polytechnic University, China^b School of Geosciences and Info-physics, Central South University, China

ARTICLE INFO

Keywords:

Mangla reservoir
Reservoir-associated earthquake
InSAR
Décollement
Hydrological loadings

ABSTRACT

The extreme rainfall weather during the Indian monsoon season has increased in recent decades changing the hydrological mass distribution that may be responsible for triggering regional earthquakes. In the western Himalayas, a shallow M_w 5.7 earthquake took place right after the withdrawal of the 2019 unusual Indian summer monsoon resulting in a rapid increase of $\sim 4.5 \text{ km}^3$ of water storage at the nearby Mangla reservoir within three months. Through a joint inversion of space geodetic and telesismic data, we found that the mainshock occurred on the décollement structure of the Main Himalayan Thrust in the western Himalayas, which was previously underdetermined. The significant water loading, and pore pressure diffusion led to Coulomb stress increases of $\sim 10 \text{ kPa}$ on the maximum coseismic slip zone promoting fault failure. Our findings demonstrate that climate change could influence certain reservoir-associated earthquakes in the Himalayas. We provide recommendations to improve the regulations for the reservoir operations in Mangla and probably other contexts with similar tectonic settings in the Himalayas during the monsoon season.

1. Introduction

Reservoir-associated earthquakes typically occur during the initial impoundment periods (e.g., Kremasta and Nurek reservoirs) or the first several filling and emptying cycles (e.g., Koyna and Hoover reservoirs) due to the change in stress regime from the combined effect of large vertical stress change and pore pressure diffusion (Gupta, 1985; Simpson, 1986; Talwani, 1997). However, on September 24, 2019, an earthquake of M_w 5.7 struck $\sim 10 \text{ km}$ southeast of the Mangla dam in Pakistan (Fig. 1, National Earthquake Information Center, 2019), which was safely operated for >50 years without $M>5.0$ earthquakes (Fig. 1c; Adams and Ahmed, 1969; Brown, 1974; Kayani, 2013).

Tectonically, the Mangla reservoir is located close to the Hazara Kashmir Syntaxis (HKS), which is one of the most active syntaxis systems in the NW Himalayas (Fig. 1a; Treloar and Coward, 1991; Avouac et al., 2006). The transforming orientation of collision and suturing between the Indian and Eurasian plates resulted in a strong curling and fold pattern and earthquake nucleation, including the devastating 2005 M_w 7.6 Muzaffarabad earthquake (Hussain and Yeats, 2009; Shah et al., 2020). However, few noticeable seismicity ($M_w>5.0$) has been documented since 1966 (ISC catalog; Brown, 1974) in the core and southern

part of HKS, near the Salt Range Thrust (SRT) and Kohat-Potwar Plateau, except for the 1992 M_w 6.0 Kohat earthquake in the western part of the SRT (Satyabala et al., 2012) and the 2006 M_L 5.0 New Mirpur earthquake, located $\sim 7 \text{ km}$ SE of Mirpur city (Iqbal et al., 2009). The presence of a thick salt layer surrounding the SRT and overlying the possible basal décollement may explain the cumulative stress release (Satyabala et al., 2012), which is consistent with the caterpillar creeping (i.e., 1–2 mm/yr) deformation observed near the Kohat-Potwar Plateau and SRT (Abir et al., 2015).

The strongest component of monsoon systems, the Indian summer monsoon, modulates approximately 80% of the annual rainfall to South Asia, and is the major source of runoff to the Mangla reservoir during the active monsoon months (Kayani, 2013; Huang et al., 2020). In 2019, the unusual Indian summer monsoon caused an abnormal increase in precipitation in Pakistan and India from July to mid-September (Fig. 1b–c). The cumulative rainfall has reached the highest record from the past 25 years that caused a rapid water storage increase of $\sim 4.5 \text{ km}^3$ at the Mangla reservoir. The 2019 event occurred during the transition period between the peak value and the water release period in mid-September (Fig. 1b). This coincidence poses the question of whether the occurrence of an event is linked with unusual weather (Sharma et al., 2020).

* Corresponding author.

E-mail address: wenbin.xu@csu.edu.cn (W. Xu).

Here, we study the causality of the 2019 event using multi-remote sensing and teleseismic data. We first adopted Interferometric Synthetic Aperture Radar (InSAR) and teleseismic data to constrain the geometry of seismogenic fault and estimate the model uncertainty using Bayesian inference. It provides new evidence of the localized fault geometry of the Main Himalayan Thrust (MHT) beneath the western end of the Main Frontal Thrust (MFT). Using satellite-based optical imagery and laser data, we mapped the evolution of the reservoir's water volume before and after the earthquake. In combination with the pore pressure model and the Coulomb-Mohr failure theory, we studied the effects of rapid reservoir loading on fault stability. We suggest that the reservoir operation regulation during the summer monsoon season should be carefully arranged to avoid the potential destabilization imposed on the underlying active décollement.

2. Material and methods

2.1. Coseismic data processing

2.1.1. InSAR data

We selected two pairs of Sentinel-1A images acquired on ascending track 100 and descending track 107 (Table S1) to map the coseismic displacements. Both coseismic pairs were processed using the InSAR Scientific Computing Environment (ISCE) software (Agram et al., 2016). We applied the enhanced spectral diversity (ESD) method to guarantee a residual error of coregistration below 1/1000 pixels following the initial geometrical coregistration (Fattah et al., 2016). Then, we used the 1-arc Shuttle Radar Topography Mission (SRTM) DEM to eliminate the contribution of topography (Farr et al., 2007). We multilooked interferograms with 5 pixels in azimuth direction and 19 pixels in range direction. All interferograms were filtered using an adaptive spectral

filter (Goldstein and Werner, 1998) and unwrapped using the minimum cost flow algorithm (Chen and Zebker, 2002). We further adopted a quadratic surface to eliminate any remaining orbital error. While only evident topographic-correlated atmospheric artifacts can be observed in the ascending pair, we fitted and removed the remaining topography-phase term using a linear function (Wang et al., 2017; see Fig. S1 and Fig. 5 for the processed interferograms).

2.1.2. Teleseismic data

The 13 teleseismic stations were collected from the Incorporated Research Institutions for Seismology (IRIS) and GEO-ForschungsNetz (GEOFON) networks at epicentral distances between 30° and 90° to ensure a uniform azimuthal distribution and high signal-to-noise ratios (Fig. S2). We filtered the raw P-wave records on the vertical channel by the band-pass filter ranging from 0.01 Hz to 0.1 Hz and deconvolved P-wave to the vertical displacements. We tapered the waveform to the 95 s time window, including the data 30 s before the initial arrivals. The velocity model used in the teleseismic Green's function (i.e., the receiver's side) was referenced to the global velocity model AK135, but we substituted the shallow crust structure with CRUST 2.0, according to the locations of the selected stations (Bassin et al., 2000).

2.2. Fault inversion and modeling

We used InSAR and teleseismic data to jointly constrain the fault geometry and used the Bayesian inference to appropriately evaluate the uncertainties from the model and data simultaneously (Vasyura-Bathke et al., 2020). We first applied the quadtree subsample method (Jónsson et al., 2002) to the InSAR measurements (i.e., a total of 302 grids; Fig. S1) to reduce the computational burden and keep the nonlinear inversion solvable. We weighted the quadtree grids based on the

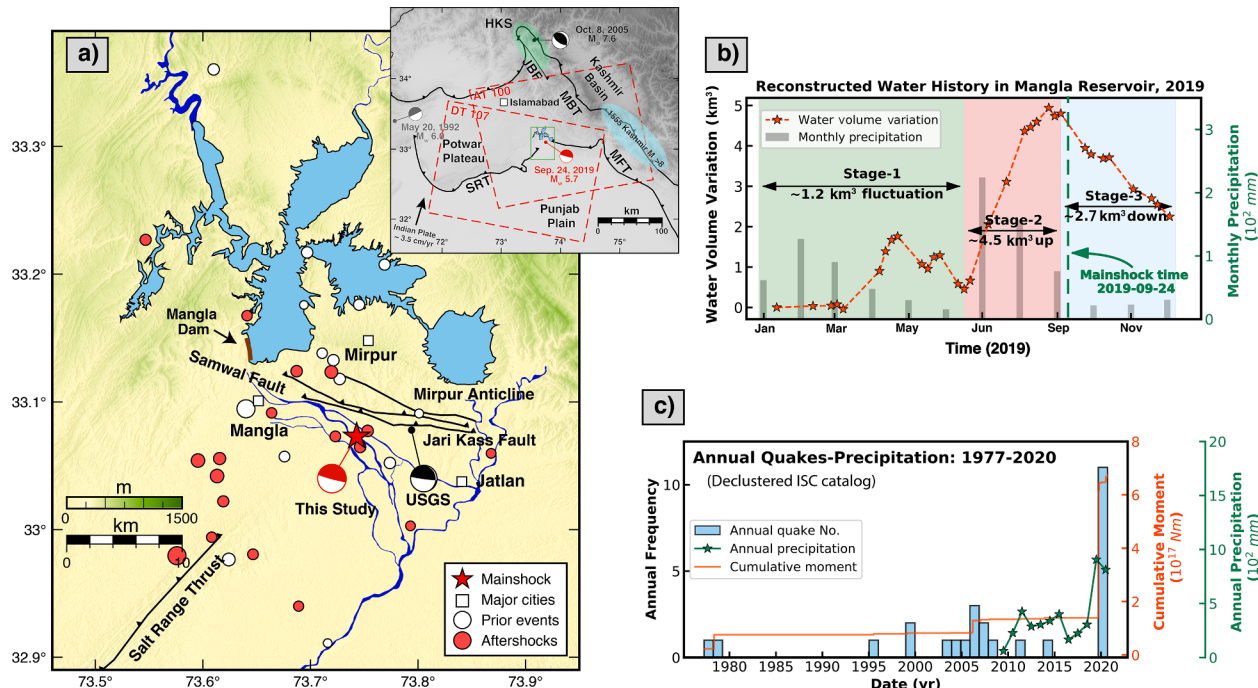


Fig. 1. Tectonic context and retrieved water history in the study area. a) Tectonic setting near the Mangla reservoir (Ahmed, 2009; Iqbal et al., 2009; Ackers et al., 2016). White circles represent the pre-2019 events from 1977, and the red circles represent aftershocks until September 2020 (ISC catalog). The inset shows the general tectonic map in north Pakistan and the data coverage (Avouac et al., 2006; Gavillot et al., 2016). The black arrow represents the plate convergence velocity (Jade et al., 2017). The red dashed rectangles denote the coverage of Sentinel-1A data (i.e., ascending track 100 and descending track 107). The green rectangle bounds the extent of a). HKS-Hazara Kashmir Syntaxis; MBT-Main Boundary Thrust; MFT-Main Frontal Thrust; JBF-Jhelum Balakot Fault; SRT-Salt Range Thrust. b) The retrieved water history from Sentinel-2 and corrected AW3D30 DEM in 2019. Red and green lines represent the water volume variation and the mainshock date, respectively. The histograms denote the monthly precipitation (World Weather Online). c) The statistics of the earthquakes and the cumulative moment from the declustered ISC catalog ($M>3.0$, declustering by Reasenberg (1985) method). The green line represents the annual precipitation in New Mirpur city during 2009–2020 (World Weather Online). (For interpretation of the references to colour in this figure legend, the reader is referred to the web version of this article.)

variability in the far-field pixels. The seismic data variances were determined by the fluctuation of the data before the P-waveform arrival time.

We employed the Bayesian Earthquake Analysis Tool (BEAT, Vasyura-Bathke et al., 2020) to perform the nonlinear inversion. Considering different independent observations $d = \{d_1, d_2, \dots, d_n\}$ and the model of the source parameters $m = \{m_1, m_2, \dots, m_k\}$, the observation equation with error ϵ is

$$d = G(m) + \epsilon \quad (1)$$

where $G(m)$ is Green's function for the transient (i.e., seismic displacement) or static displacement (i.e., geodetic displacement). In the Bayesian framework, the degree of how well a set of parameters fits the data is the uncertainty and it is expressed as follows:

$$p(m|d) = \frac{p(d|m)p(m)}{p(d)} \propto p(d|m)p(m) \quad (2)$$

where $p(m)$ is the prior probability distribution information of the model setup, and $p(d)$ is the normalization factor. $p(d|m)$ is the likelihood function that measures the goodness of fit between model predictions and observations. It quantifies the probability of a given set of parameters for data,

$$p(d|m) = L(m) = \frac{1}{(2\pi)^{n/2} |C_d|^{1/2}} \exp \left\{ -\frac{1}{2} [d - G(m)]^T C_d^{-1} [d - G(m)] \right\} \quad (3)$$

C_d^{-1} is the inverse of the variance-covariance matrix of the data for weighting the multi-source of our observations. If different observations are independent, the likelihood function for all observations is the product of Eq. (3). Because the analytic solution or approximation is not available to calculate the PPD, we constructed a discretized form of PPD through the sequential Monte Carlo (SMC) method.

Two possible earthquake nodal planes (one with a high dip angle of 87° and the other with a shallow dip angle of 12°) from the USGS W-phase solutions are likely responsible for this earthquake. Because a high-dip angle (e.g., 60°) thrust event is uncommon or even impracticable considering the prevailing thrust tectonic background in the Himalayan foreland (Sibson, 2012), we preferred a shallow dipping nodal plane to account for this event. Therefore, we set the initial search interval as strike $\in [235^\circ, 360^\circ]$, rake $\in [40^\circ, 180^\circ]$, and dip $\in [0^\circ, 20^\circ]$ taking the focal mechanism solutions in different catalogs as the priors (Table 1).

Considering the posterior probability distributions of the strike and rake angles exhibit a linear relationship (Fig. S3), we also applied the 2D grid search method to determine the unavoidable trade-off between strike and rake parameters in the low-dipping fault geometry after the first iteration of non-linear inversion (Feng et al., 2017). Hence, we fixed other parameters except the rake and strike angles and minimizing the

Table 1
Source parameters of the 2019 M_w 5.7 New Mirpur earthquake.

InSAR + Seismic	2D Grid Search	USGS	GCMT	GFZ	NSMC	NCS
Lon ($^\circ$)	$73.75_{-0.01}^{+0.02}$	73.79	73.85	73.81	73.73	73.70
Lat ($^\circ$)	$33.07_{-0.01}^{+0.01}$	33.08	33.03	33.09	32.99	33.10
Strike ($^\circ$)	$277.7_{-17.2}^{+12.4}$	278.1	352/ 98	246/ 104	250/ 74	/
Dip ($^\circ$)	$4.0_{-1.9}^{+1.9}$		12/ 87	10/81	9/81	/
Rake ($^\circ$)	$79.2_{-15.3}^{+16.7}$	83.9	164/ 78	52/96	86/ 91	/
Depth (km)	$3.9_{-0.3}^{+0.5}$		11.5	14.7	10.0	10.0
M_w	$5.72_{-0.02}^{+0.02}$		5.4	5.7	5.3	5.8

misfits between the observations and model predictions as our best-fit geometry solution (Fig. 2; Table 1).

For the linear finite slip model inversion, we assumed that the slips on adjacent patches were continuous to avoid an unrealistic stress drop (Amey et al., 2018). Therefore, we regularized the linear inversion by applying the Laplacian constraint to stabilize the distributed slip (1×1 km patches). We used the sequential Monte Carlo (SMC) method to obtain the maximum-a-posterior (MAP) solution for the dip-slip and strike-slip in each patch, and the degree of Laplacian smoothness and scaling parameter (Vasyura-Bathke et al., 2020; see the finite slip model in Fig. 6).

2.3. Water history reconstruction

To reconstruct the long-term water history in the reservoir, we used Landsat-5, Landsat-7, Landsat-8, and Sentinel-2 imagery (Fig. S4) with fine temporal resolution and cloud cover of less than 20% to extract the water area from 1987 to 2019. We employed the modified normalized difference water index (MNDWI; Xu, 2006) to delineate the water area. The threshold for this two-class segmentation task was determined using Otsu's method (Otsu, 1979). We assumed that the varying lakeshore lines extracted from the water area could reflect the water level across the entire reservoir. Therefore, we estimated the water level and volume variation of the reservoir by delineating the inundated water area and the DEMs (Tseng et al., 2016). We evaluated the accuracy of the accessible DEMs with ~ 30 m resolution in the Mangla reservoir, including the ALOS World 3D-30 m (AW3D30), Advanced Spaceborne Thermal Emission and Reflection Radiometer Global Digital Elevation Model (ASTER-GDEM), and 1-arc SRTM (Table S2). These DEMs may not accurately reflect the regional landscape and need alignment before feeding into the water level/volume estimation (Madson and Sheng, 2020). Hence, we accounted for the ICESat-2 (Ice, Cloud, and land Elevation Satellite), with 5–10 cm vertical accuracy on 100-m segments (Li et al., 2019), as a reference for our disposal (Kropáček et al., 2012). We compared the absolute mean differences and variances between the strong beam pulses of the ICESat-2 ATL08 (land water vegetation elevation) measurements (Fig. 3) and the three DEMs. We found that the AW3D30 DEM outperformed with a lower mean absolute difference and standard deviation (Fig. 3e). Therefore, we finally applied the AW3D30 DEM and aligned the DEM with the average difference from the ICESat-2 results.

2.4. Coulomb stress modeling from reservoir's loading

We employed the Coulomb-Mohr theory to evaluate the reservoir's role in earthquake occurrence and modeled Coulomb stress change to quantify fault stability. The change in the Coulomb stress driven by the reservoir's filling/emptying cycles can be formulated as a combination of the stress change and coefficient of friction μ :

$$\Delta S = \Delta \tau - \mu(\Delta \sigma - \Delta P) \quad (4)$$

where $\Delta \sigma$ and $\Delta \tau$ are the normal and shear elastic stress changes directly from the mass variations in the reservoir, respectively. Conventionally, we defined the compressive $\Delta \sigma$ as positive. We estimated the normal stress change $\Delta \sigma$ and shear stress change $\Delta \tau$ using the Boussinesq solution (Jaeger and Cook, 2009) and resolved them on the inverted fault geometry (strike = 278.1° , dip = 4.0° , rake = 83.9° , Table 1).

According to Roeloffs' theory (Roeloffs, 1988), the change in pore pressure ΔP near the reservoir can be expressed as the summation of the compression-driven term ΔP_c and diffusion-driven term ΔP_d as $\Delta P = \Delta P_c + \Delta P_d$. The instantaneous effect of pore pressure change due to compression/tension is proportional to the summation of the normal stress change, as follows:

$$\Delta P_c = B \left(\frac{\sigma_{xx} + \sigma_{yy} + \sigma_{zz}}{3} \right) \quad (5)$$

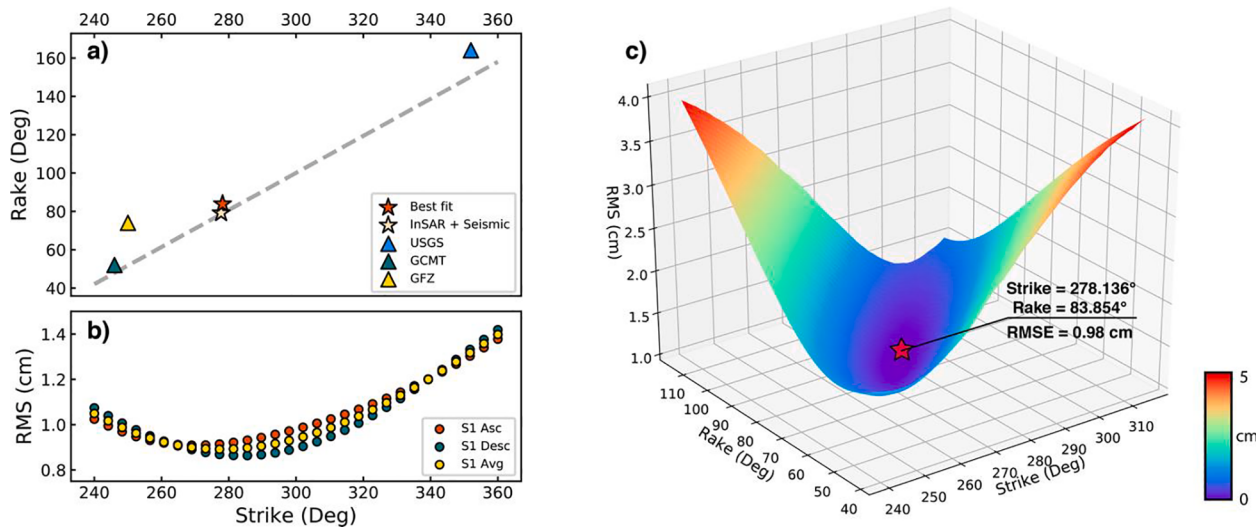


Fig. 2. Results of 2D grid search. a) The linear relationship between strike and rake angles from our joint inversion solution and other catalogs (i.e., shallow dipping nodal planes). b) The corresponding misfit (RMS) between the homogenous fault models and the observations. c) 2D fitting plane using grid search to refine the trade-off between rake and strike angles.

where B is the Skempton's coefficient representing the ratio of the pore pressure change and the mean stress change. The diffusion process of pore pressure is followed by the Biot Law (Biot, 1941), and the corresponding differential equation is:

$$c\nabla^2(\Delta P_d) - \frac{\partial}{\partial t}(\Delta P_d) = S(x, y, z, t) \quad (6)$$

where $S(x, y, z, t)$ is the water history of the point load at location (x, y, z) on time epoch t due to the reservoir operation, and c is the hydraulic diffusivity representing the diffusion speed of pressure redistribution. We adopted Green's function solution from Kalpana and Chander (2000) to solve the diffusion term ΔP_d in a porous elastic half-space. To test different diffusion speed scenarios, we set the hydraulic diffusivity to $0.5 \text{ m}^2/\text{s}$, $2 \text{ m}^2/\text{s}$, and $5 \text{ m}^2/\text{s}$ (Fig. 7 and Fig. S5). Finally, we changed the dip angle from 0° to 90° to study the sensitivity of different dip angles to the stress field (Fig. S6).

3. Results

3.1. Water variations in the reservoir

In recent three decades, the amplitudes and phases of the retrieved water variations indicate that the reservoir operation can be classified into two periods (Fig. 4). The first period (i.e., 1987–2012) shows that the water fluctuates between 340 m to 360 m, corresponding to $\sim 3.0 \text{ km}^3$ water volume change. In the second period (i.e., 2013–2019), the average peak-to-valley (PV) water level is ranging from 341 m to 368 m (Fig. 4a). Correspondingly, the average PV water volume variation is $\sim 4.5 \text{ km}^3$, accounting for a 50% increase from 1987 to 2012 (Fig. 4b). We suggest that this annual increment of impoundment (i.e., $\sim 8 \text{ m}$) should be related to the dam raising project completed in December 2009, in which the main dam has 9 m (~ 30 feet) heightening to enhance the water storage and electricity generation (Kayani, 2013).

In 2019, the water storage at the Mangla reservoir was at the relatively low level of $\sim 0.5 \text{ km}^3$ at the end of June. A massive rainfall started in July, which caused a rapid water level increase at the Mangla reservoir. The reconstructed water history from ICESat-2, optical images, and external DEM shows that the Mangla reservoir experienced three water variation stages in 2019 (Fig. 1b; Fig. 3a). The reservoir first shows a $\sim 1.2 \text{ km}^3$ water volume fluctuation for the regular watershed management from January to June, including one small precipitation peak in

March and the subsequent snow/glacier melting (Babur et al., 2016). During the 2019 summer monsoon season, the water level drastically increased from $\sim 348 \text{ m}$ to 371 m , which is equivalent to $\sim 4.5 \text{ km}^3$ loading of the crust. This water volume surge in 2019 is the historic water gain during the monsoon season (i.e., June to September) in the recent three decades (Fig. 4d). In the middle of September, the water level (i.e., 371 m) is reaching a record high and beyond the two sigma limits on the basis of the three decades observations (i.e., $351.3 \pm 18.3 \text{ m}$). The third water variation stage is from mid-September to the end of 2019, during which the reservoir experienced a $\sim 12 \text{ m}$ water level decrease, corresponding to $\sim 2.7 \text{ km}^3$ of storage change. These estimated water level changes match well with the direct ICESat-2 measurements and Landsat-8 estimations (Fig. 3c-d), with a strong value of 0.99 (Fig. 3d). The major difference between ICESat-2 measurements and estimations is observed between April and June (Fig. 3c), in which the ICESat-2 did not have data coverage.

3.2. Coseismic deformation of the 2019 event

The coseismic interferograms show consistent north–south complementary deformation lobes (Fig. 5). As the SAR satellites observe the surface deformation in the line-of-sight (LOS) direction, these comparative deformation patterns suggest that the coseismic deformations are dominated by fault thrust slip (Elliott et al., 2016), which agrees well with the thrust tectonic background. The northern lobe is likely to represent an away-from-satellite ground motion (i.e., subsidence) and the southern lobe movements toward the satellite (i.e., uplift) (Fig. 5a, d). These apparent symmetric double-lobe patterns with no apparent surface rupture observed from the interferograms suggest that the mainshock occurred on a W-E oriented blind seismogenic fault. The ascending coseismic interferogram shows a maximum coseismic LOS displacement of $\sim 9.6 \text{ cm}$ in the southern deformation lobe, while the descending interferogram is degraded by the low coherence due to the longer temporal baseline (Table S1) with only up to $\sim 6.5 \text{ cm}$ LOS displacement observed in the southern part. The maximum deformation area in the descending pair is shifted by approximately 4 km to the east compared to the ascending interferogram. This is due to the different viewing geometries of the different orbits.

3.3. Fault geometry and slip distribution

We used InSAR and teleseismic data to conduct a non-linear inver-

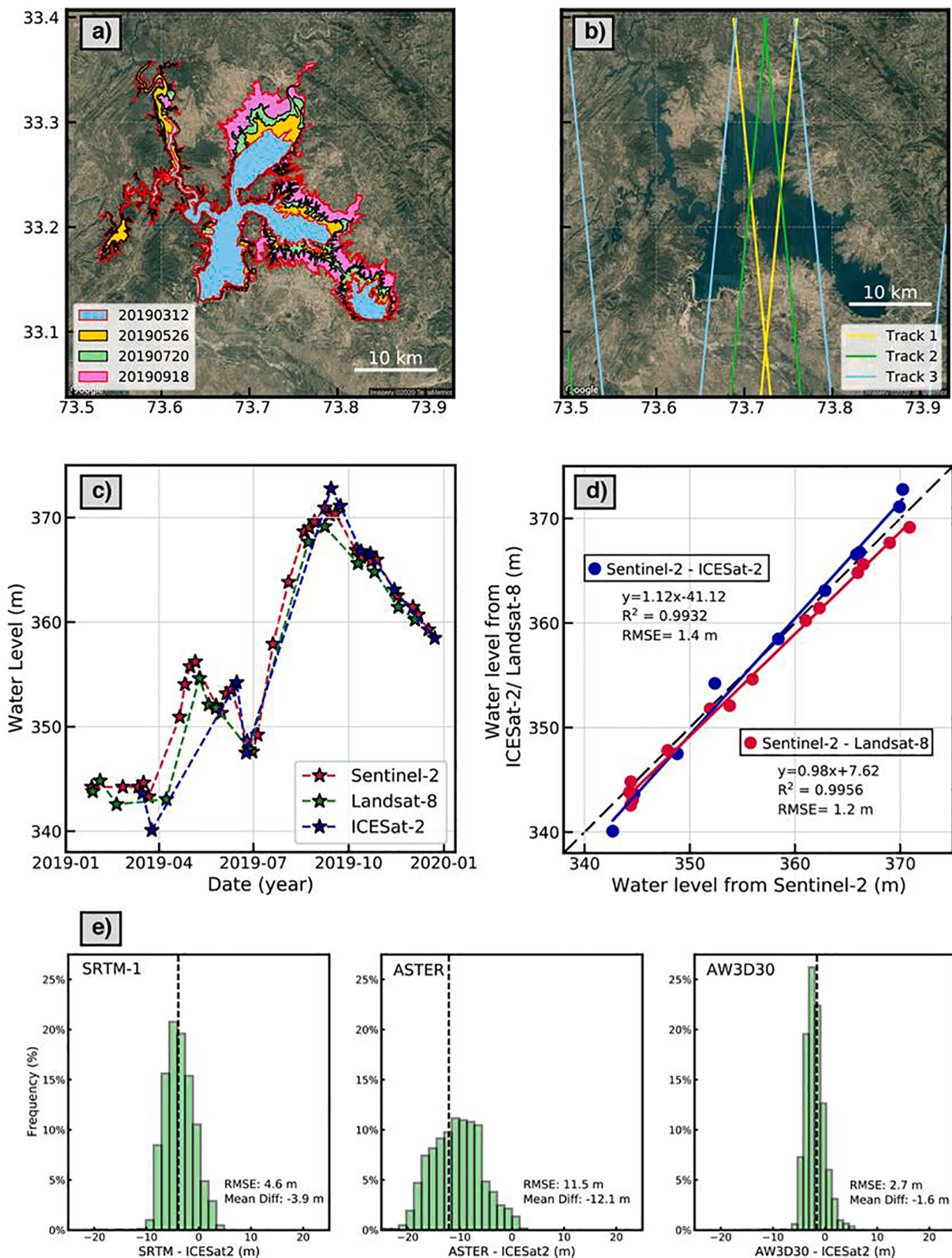


Fig. 3. Water parameter estimation and validation. a) An example of the water area variations during March-September from Sentinel-2 imagery (prior to the mainshock). b) Ground tracks of ICESat-2 strong beams in the New Mirpur area (both ascending and descending). c) The water level estimations from Sentinel-2, Landsat-8 and AW3D30 DEM, and the measurements from ICESat-2 in 2019. d) The linear correlation between the Sentinel-2, Landsat-8, and ICESat-2 in 2019. e) Histograms of elevation error and statistics between different DEMs and ICESat-2.

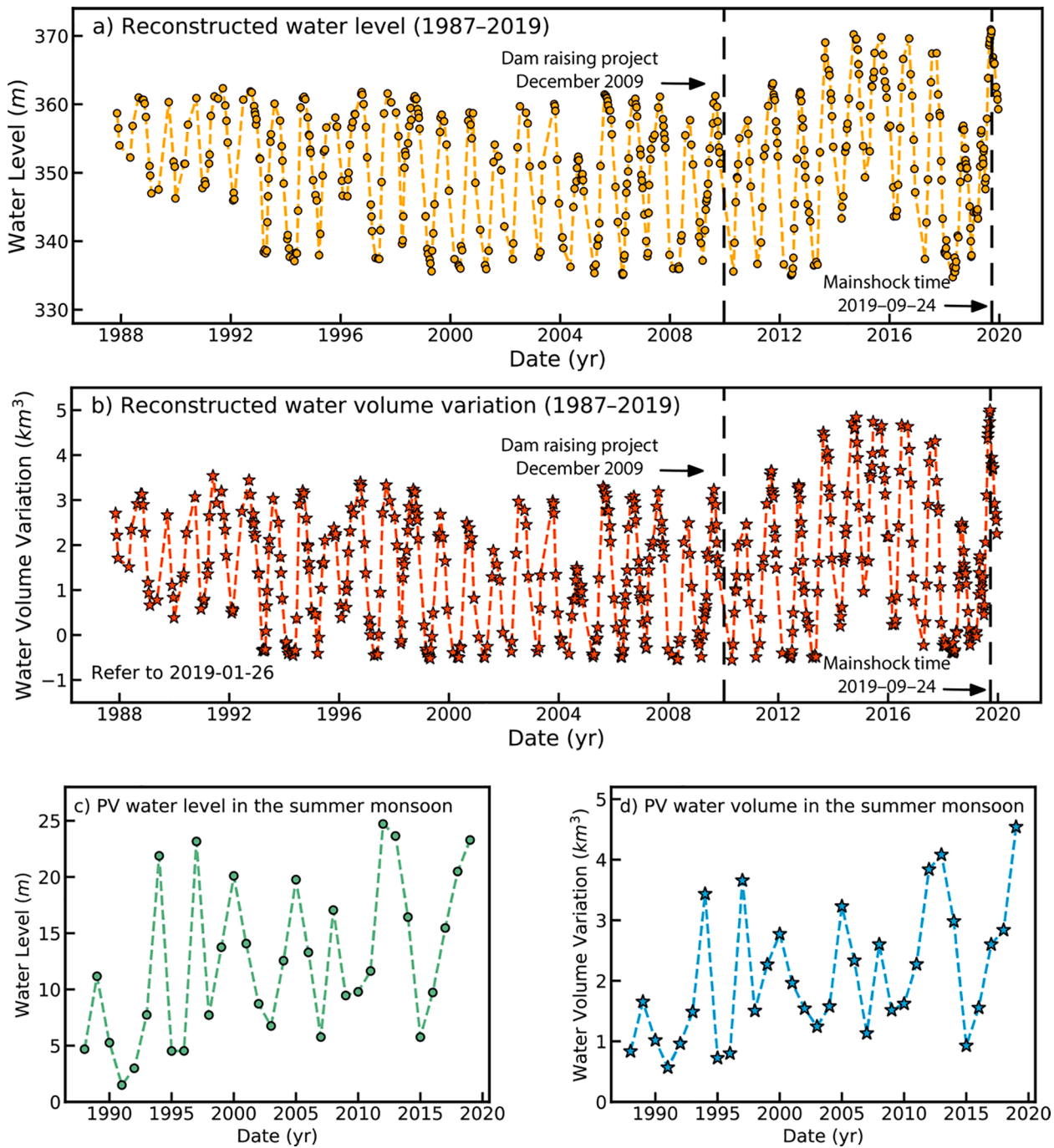


Fig. 4. The estimations of water variations in Mangla reservoir (1987–2019). a) The estimation of water level; b) The water volume variations (refer to the acquisition at 20190126); c) and d) The peak-to-valley values of water variations during the summer monsoon season (i.e., June to September).

sion under Bayesian inference, followed by a refined grid-search method to estimate the source parameters. The best-fitting finite fault slip model shows that fault rupture is mainly concentrated on a $\sim 7 \times 9 \text{ km}^2$ slip zone at depths from 4.3 km to 5.1 km dipping 4.0° to NE (Fig. 6; see Table 1 for the model uncertainty). The slip motion is dominated by a reverse fault slip with a minor left-lateral strike-slip component. The maximum slip of 0.52 m occurred beneath the north of the upper Jhelum Canal at 4.6 km depth, where the largest damage was found at the surface (Salman et al., 2019). The modeled interferograms match the InSAR observations well with RMS of $\sim 0.7 \text{ cm}$ (Fig. 5c, f). Assuming a shear modulus as 30 GPa, the estimated moment magnitude $M_w = 5.72$ is equivalent to the moment release as $M_0 = 4.27 \times 10^{17} \text{ Nm}$. In general, this moment magnitude estimation is consistent with both global

and local seismological solutions (Table 1).

3.4. Coulomb stress model

The modeled stress changes due to the water volume change of $\sim 4.5 \text{ km}^3$ during the 2019 summer monsoon season show that shear stress change $\Delta\tau$ (destabilized effect) and normal stress $\Delta\sigma$ (stabilized effect) provide opposite contributions to the fault stability (Fig. 7a–b). The stress field along variable dip angles indicates that the shear stress dominates the Coulomb stress change in a shallow dipping thrust ($0\text{--}12^\circ$), and the destabilized effect is canceled out until 30° (Fig. S6). Therefore, in our shallow dipping thrust (i.e., near the maximum slip zone), the shear stress component is ~ 2 kPa larger than the normal

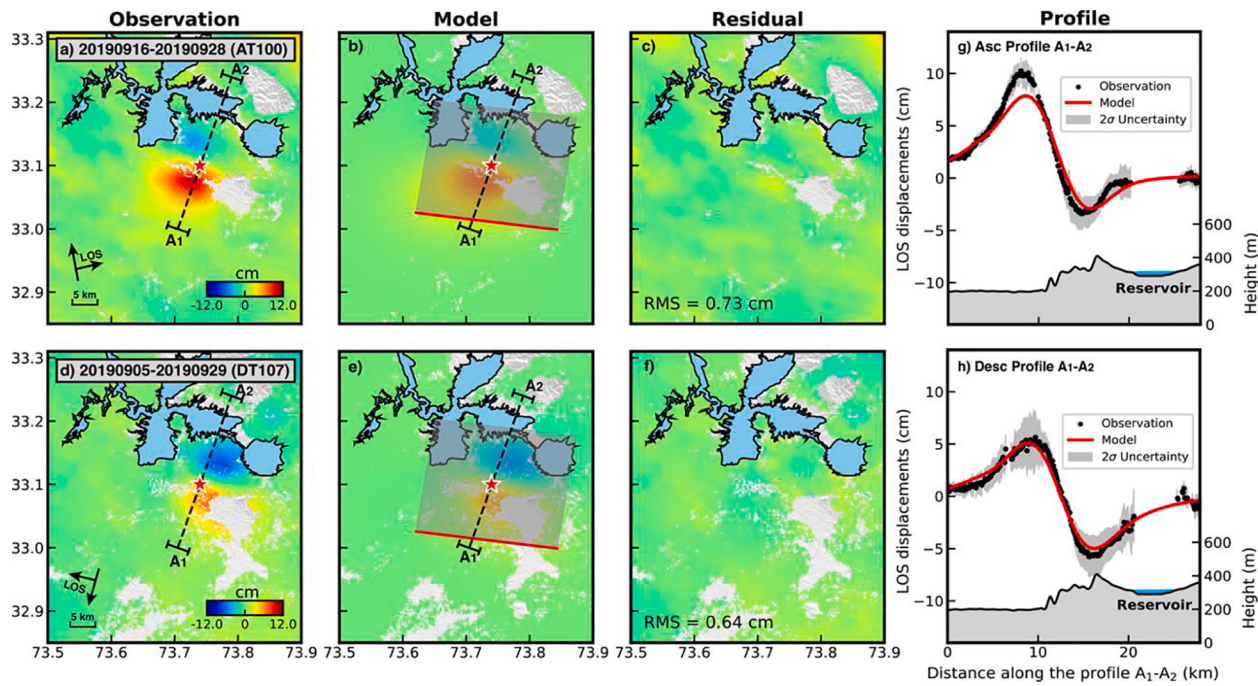


Fig. 5. InSAR observations and model predictions. The coseismic interferograms, finite slip model predictions, residuals, and LOS displacements along with the profile A₁-A₂ for ascending and the descending tracks, respectively (The warm and cold colormap represents surface movements close-to and away from the satellites, respectively).

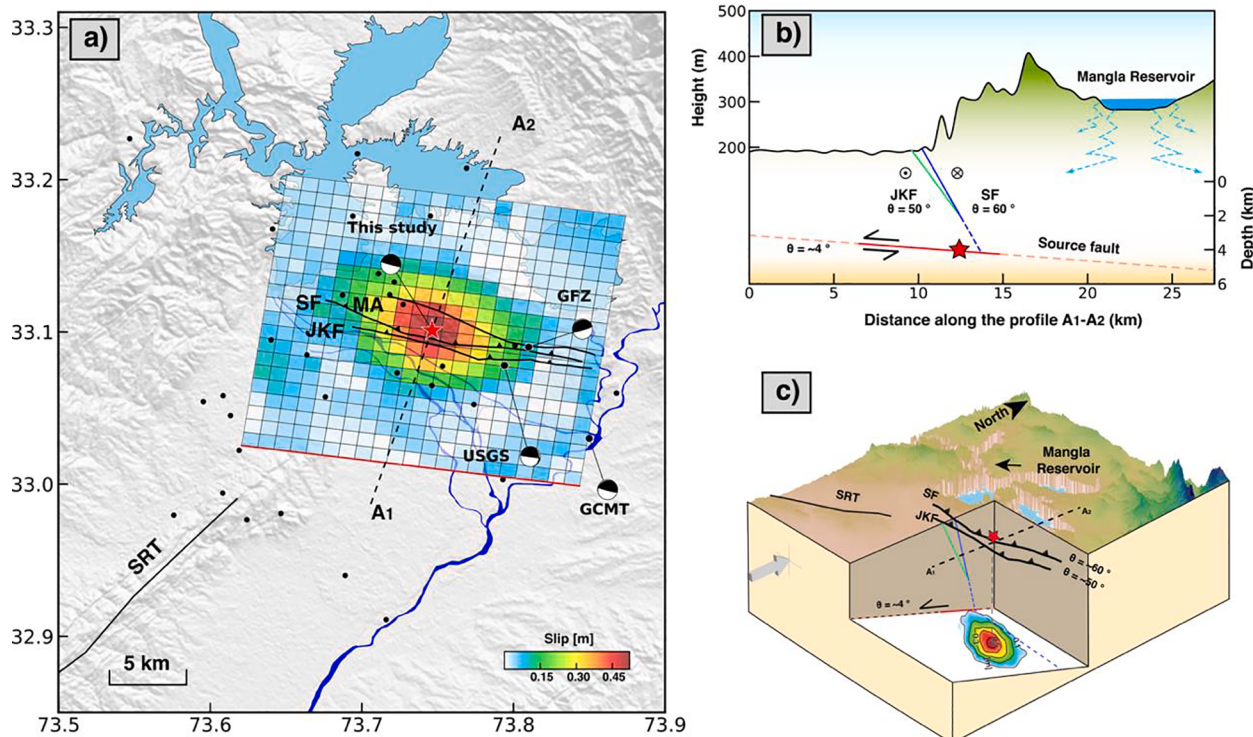


Fig. 6. The finite slip distribution and conceptional fault models. a) The surface projection of coseismic slip distribution with 1×1 km patches. The black dots represent the earthquakes with magnitudes larger than 3.0 in the ISC catalog (1977–2020). b) The 2D conceptional fault model on the profile A₁-A₂, the red, green, blue lines indicate the seismogenic fault, JK_F, the SF, respectively. The dashed red line overlying the seismogenic fault represents the section without substantial slip motion. The dashed blue line indicates the possible connection of JK_F and SF to the source fault. The dashed sky-blue arrows are the conceptual illustration showing the reservoir loading impacts. c) The 3D conceptional fault model similar to b). Note that the height and depth of the terrain in subplots b) and c) are not on the same scale for the visualization. (For interpretation of the references to colour in this figure legend, the reader is referred to the web version of this article.)

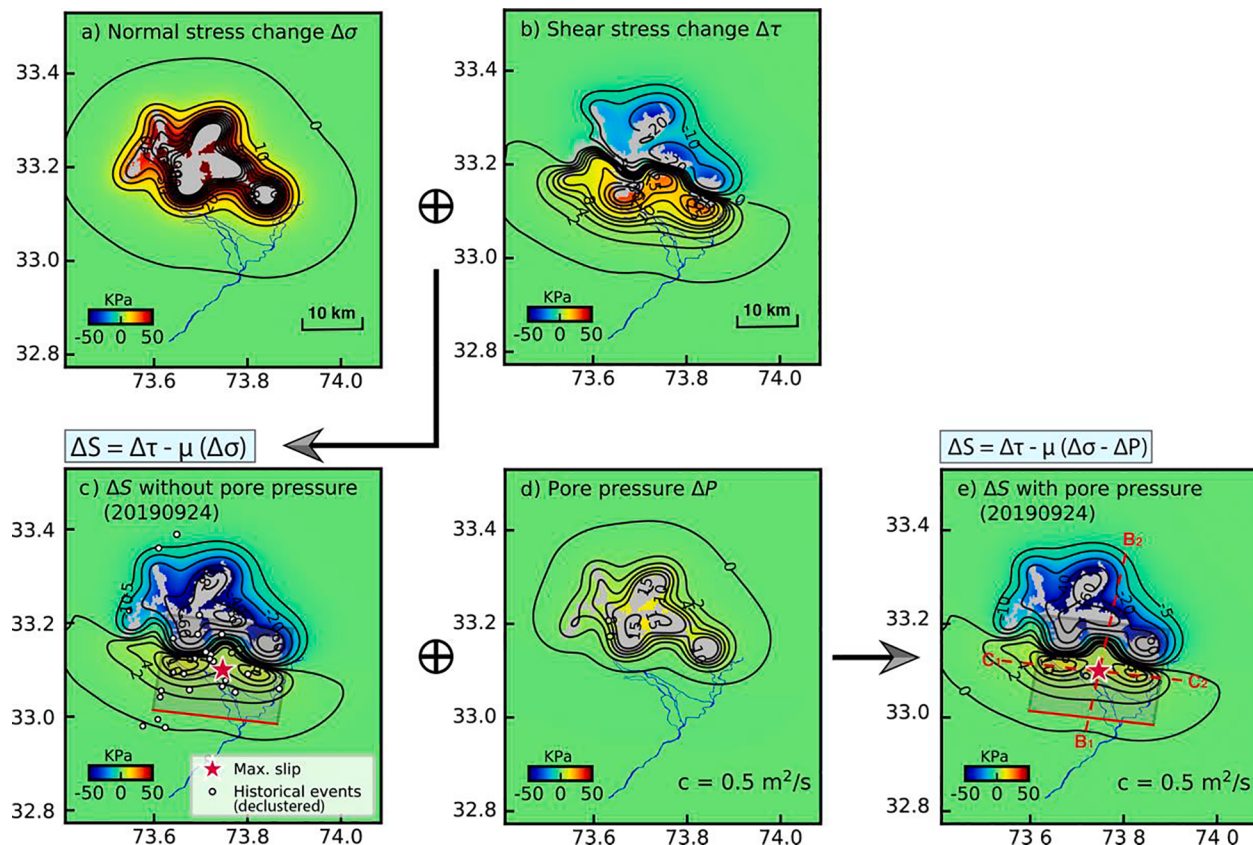


Fig. 7. Coulomb stress change on the source fault plane during the 2019 monsoon period. a) normal stress change $\Delta\sigma$; b) shear stress change $\Delta\tau$; c) ΔS from direct reservoir loading; d) pore pressure change ΔP ; e) ΔS with reservoir loading and pore pressure diffusion effect. The red star represents the location of maximum slip patch ($\sim 73.75^\circ E, 33.10^\circ N$). The white dots are the historical earthquakes from the declustered ISC catalog (1977–2020). The red dashed lines represent two selected profiles B_1-B_2 and C_1-C_2 . (For interpretation of the references to colour in this figure legend, the reader is referred to the web version of this article.)

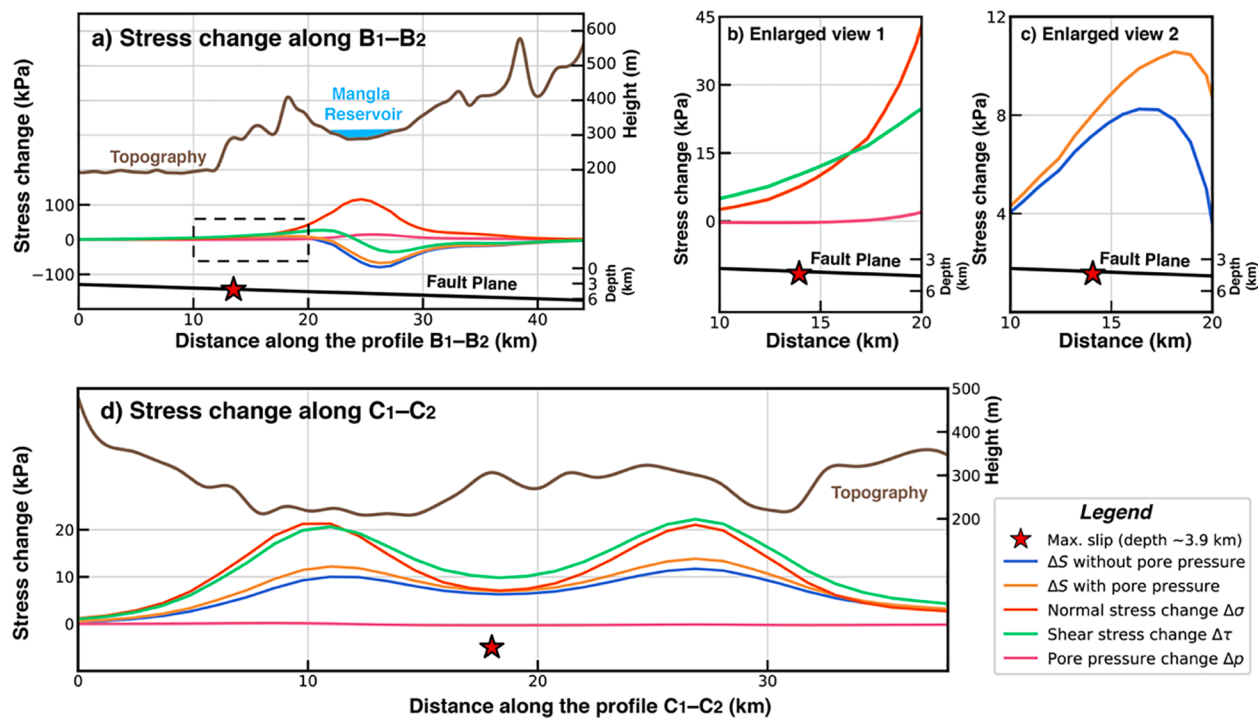


Fig. 8. Coulomb stress changes along two selected profiles. a) the stress changes along the profile B_1-B_2 ; b)-c) the enlarged view near the maximum slip area (i.e., 10–20 km along B_1-B_2); d) the stress change along the profile C_1-C_2 .

stress component, destabilizing the underlying seismogenic fault (Fig. 8b). Correspondingly, calculated Coulomb stress changes show that the maximum coseismic slip zone is located within the destabilized area with a loading induced ΔS of ~ 7 kPa (Fig. 7c; Fig. 8c). Two peaking ΔS increase zones (i.e., >10 kPa) exist at ~ 7 km near the maximum slip area along the striking profile C₁-C₂ (Fig. 8d). Considering the pore pressure diffusion process, the mean value of the pore pressure diffusion effect on the asperity ranged from 0.6 kPa to 4.3 kPa under different hydraulic diffusivities from 0.5 to 5 m²/s (Fig. 7e; Fig. S5b, g). Consequently, the pore pressure effect amplified the Coulomb stress applied to the fault plane and the total ΔS could reach as high as 15–25 kPa with the increased diffusion speed (Fig. S5b, g).

4. Discussions

During the 2019 summer monsoon season, the abnormal heavy rainfall caused a historic increase of ~ 4.5 km³ hydrological loads in the Mangla reservoir (Fig. 1b–c). This hydrological forcing alters the stress state of the subsurface and decreases the stability of the underlying thrust by two principal mechanisms: direct surface loading and pore pressure diffusion (Talwani, 1997; Johnson et al., 2017). Specifically, our stress model shows that the compressive normal stress increases the effective stress to discourage the fault slip (Fig. 7a), but the shear stress and pore pressure overcome this frictional resistance (Fig. 7b, d). Consequently, the Coulomb stress changes with or without pore pressure diffusion show consistent favoring impacts of 7–10 kPa at the maximum slip region, confirming the substantial destabilization from reservoir loading to the dislocation source (Fig. 7; Fig. S5e, j). The pore pressure estimation in our model has ambiguity associated with the hydraulic diffusivity c and the Skempton's coefficient B (Gahalaut and Hassoup, 2012). However, as the compressional term ΔP_c is much smaller than the diffusion term ΔP_d , the values of B do not make a substantial quantitative difference in our model. Even under a more permeable formation, the monotonic increase in pore pressure diffusion is supposed to maintain the extent of the destabilized zone (Zhai et al., 2019). In addition, the comparative peak Coulomb stress variation in Mangla at 15–25 kPa is comparable to other confirmed reservoir triggering events at 2–30 kPa (Gahalaut and Hassoup, 2012; Tuan et al., 2017; Gahalaut et al., 2018), supporting the mechanism of loading triggering earthquakes if the source fault has already been stressed (Shi et al., 2013).

The loading triggering mechanism contrasts with previous investigations at the Mangla reservoir, in which the prevailing EW thrust system is supposed to increase the effective stress and dominate the fault stability, thereby driving the fault away from the failure (Adams and Ahmed, 1969; Brown, 1974). However, shear stress is sensitive to the dip angle and may destroy the fault stability when the loading forces on the hanging wall of a shallowly dipping thrust (Roeloffs, 1988; Talwani, 1997). In a 2D numerical model, a new destabilizing area falls in the up-dip direction when the fault plane is shallowly dipping at 20° (Roeloffs, 1988). Similarly, we find that when the inferred thrust dips to 0–12° beneath the Mangla reservoir, the shear stress modulates the Coulomb stress and encourages the slip in the up-dip direction of the seismogenic thrust (i.e., south of the reservoir) (Fig. 7; Fig. S6). This shear stress modulated phenomenon and destabilizing in the up-dip direction is consistent with modeling and observation in the Tehri reservoir, central Himalayas (Gahalaut et al., 2018). The impoundment of the Tehri reservoir exhibits a similar destabilizing area (i.e., positive ΔS zone) in the south of the reservoir when the loading is acting on the hanging wall and resolved to MHT (i.e., dipping to 5°). The local seismic network in Tehri also confirms that most post-impoundment earthquakes are localized at the Coulomb stressing area. Similar to Tehri reservoir, the declustered ISC catalog shows that two-thirds of records (i.e., 20) in Mangla are situated in the positive ΔS zone and 12 events among them are located in the area with $\Delta S > 2$ kPa (Fig. 7c).

Therefore, the occurrence of the loading destabilizing effect in a thrust environment requires two conditions (Roeloffs, 1988): 1) the

reservoir is located on the hanging wall of a thrust fault plane, and 2) the candidate thrust fault plane is subject to a shallow dipping geometry. These two requirements and the wide extent of MHT along the Himalayan arc draw additional attention to the seismic hazards in the Himalayan foothills (Avouac et al., 2006), which is generally regarded as a reservoir loading safety area (Gupta and Rajendran, 1986). The regional seismic hazards will be underestimated (e.g., Bhakra reservoir and Pong reservoir) if we only consider seismic hazards associated with the steep major Himalayan thrusting systems with dip angles of $\sim 30^\circ$ (e.g., MBT and MCT), but ignore reservoir loading-induced shear stress increases on the shallow dipping thrust (e.g., MHT) (Gupta and Rajendran, 1986; Robert et al., 2009).

Furthermore, the physical mechanical linkage between mass redistribution due to the Indian summer monsoon and earthquake occurrence is not limited to reservoirs. Various monsoon-related local hydrological loading and monsoon-induced disasters are expected to modulate the seismicity. For the direct loading dominant mechanism, it is commonly acknowledged that the monsoon-induced surface hydrological loading in the Ganges Basin modulates the seasonal seismicity rate on the MHT (Fu and Freymueller, 2012). The rapid inflow from the surface loading may also change the distribution of groundwater in the subsurface aquifer. As a consequence, elastic rebounds due to the mass redistribution of groundwater may result in the extra stress perturbation on the seismogenic fault (González et al., 2012; Oestreicher 2018). Extreme weather during the monsoon season may also change the landscape due to erosion, landslides, and barrier dams, which are capable of decreasing the subsurface effective stress, favoring the slip along the specific fault planes (Steer et al., 2014; Chang et al., 2018). For the pore pressure diffusion modulated principle, monsoon-induced heavy rainfall and flooding cause a transient concentration of surface water flux and groundwater recharge, resulting in pore pressure diffusing to the source fault or decreasing the friction coefficient to encourage the slip motion (Hainzl et al., 2006, 2014). This was observed in the 2018 Kerala Flood, India. Monsoon rainfall increases the seismic risk by the infiltration of pore pressure, which decreases the effective stress (Ramasamy et al., 2019). Similarly, the transient heavy rainfall in Palghar, India, during the 2019 abnormal monsoon season is deemed to be responsible for the reactivation of the earthquake swarm due to the pore pressure diffusing into the permeable fracture zone (Sharma et al., 2020). As the local precipitation data shows a substantial increase in 2019 (Fig. 1c), we speculate the hydraulic loading in the local aquifer may also influence the earthquake occurrence due to the fluid flow in the filled pore spaces from the differential pressure (Hu and Bürgmann, 2020). We suggest more in-situ data including the local aquifer stratification, the well data, GNSS data, and local seismic network are needed to map the accurate regional hydrological changes and decipher the modulation between the earthquake, reservoir operation and local aquifer system (Johnson et al., 2017; Hsu et al., 2021).

In contrast to MHT in the central Himalayas, which has been thoroughly investigated (Duputel et al., 2016; Elliott et al., 2016; Xu et al., 2016; Feng et al., 2017), the lack of surface rupture near the eastern SRT results in the remaining blind of localized MHT structure (Thakur et al., 2010). Our fault model shows that the fault plane dips gently from $\sim 4.0^\circ$ to the northeast at a depth of ~ 4.6 km (Fig. 6). This closely resembles a basal décollement structure beneath the foreland of the SRT (i.e., ramping part of the MFT; Rehman et al., 2016; Ghani et al., 2018). Beneath the Potwar Plateau and SRT, seismic profiles suggest that the décollement structure is 3–5° northward dipping and partly linked with SRT (McDougall and Hussain, 1991; Chen and Khan, 2010). If we consider the MHT depth revealed near the Kashmir valley at 8–15 km (Paul et al., 2018), the MHT depth in front of the Mangla reservoir is 2–9 km, which is in accordance with our estimation. The thinning of the salt layer between SRT and JBF from the in-situ survey and seismic reflection provides further evidence for the possible rupture of this grounded seated décollement (Davis and Engelder, 1985; Pennock et al., 1989). Therefore, our model provides compelling evidence for the MHT

décollement structure beneath the western terminus of the MFT (i.e., northeast of the SRT).

5. Conclusions

Our analysis of satellite optical and laser data covering the Mangla reservoir at the east flank of SRT in the western Himalayas demonstrates that the heavy rainfall during the 2019 Indian summer monsoon has caused a historic water volume increase of $\sim 4.5 \text{ km}^3$ at the Mangla reservoir. This significant mass change has increased up to 25 kPa Coulomb stress on the shallow décollement beneath the western end of the MFT, which is responsible for the 2019 $M_w 5.7$ earthquake. As extreme weather events from summer monsoons become more frequent in South Asia due to climate warming, the techniques and analyses presented here can help monitor unusual reservoir level changes and assess potential seismic hazards in densely populated and ecologically vulnerable regions.

CRediT authorship contribution statement

Lei Xie: Writing - original draft, Methodology, Investigation, Visualization. **Wenbin Xu:** Conceptualization, Investigation, Methodology, Writing - review & editing, Supervision. **Xiaoge Liu:** Writing - review & editing. **Xiaoli Ding:** Writing - review & editing, Supervision.

Declaration of Competing Interest

The authors declare that they have no known competing financial interests or personal relationships that could have appeared to influence the work reported in this paper.

Acknowledgments

We greatly thank the Editor, the Associate Editor and the two reviewers for their constructive comments that greatly helped us to improve our manuscript. We would like to thank Dr. Hannes Vasyura-Bathke (University of Potsdam) for detailed suggestions and instructions on using BEAT (<https://hvasbath.github.io/beat>). We thank Prof. Kalpana Gahalaut and Dr. Thai Anh Tuan (National Geophysical Research Institute, India) for the discussion and suggestion in stress modeling. We also thank Prof. Muhammad Basharat and Fahad Hameed (University of Azad Jammu & Kashmir) to provide the regional geomorphologic information. The research is supported by the National Key R & D Program of China (2019YFC1509205) and the National Natural Science Foundation of China under Grant No. 41804015. Sentinel-1A data was acquired from the Alaska Satellite Facility (<https://www.asf.alaska.edu/>). Sentinel-2 and Landsat imageries were collected from Google Earth Engine Data Catalog (<https://developers.google.com/earth-engine/datasets>). ICESat-2 data was downloaded from National Snow & Ice Data Center (<https://www.nsidc.org>). Precipitation data was obtained from World Weather Online (<http://www.worldweatheronline.com/>). Some figures were prepared by the Generic Mapping Tools 6.0 (Wessel et al., 2019) and Salem Library (Maussion et al., 2020).

Appendix A. Supplementary material

Supplementary data to this article can be found online at <https://doi.org/10.1016/j.jag.2021.102401>.

References

- Abir, I.A., Khan, S.D., Ghulam, A., Tariq, S., Shah, M.T., 2015. Active tectonics of western Potwar Plateau-Salt Range, northern Pakistan from InSAR observations and seismic imaging. *Remote Sens. Environ.* 168, 265–275.
- Ackers, J., Hieatt, M., Molyneux, J.D., 2016. Mangla reservoir, Pakistan—approaching 50 years of service. *Dams Reservoirs* 26, 68–83.
- Adams, R.D., Ahmed, A., 1969. Seismic effects at Mangla dam. *Pakistan. Nat.* 22, 1153–1155.
- Agram, P.S., Gurrola, E.M., Lavalle, M., Sacco, G.F., Rosen, P.A., 2016. The InSAR Scientific Computing Environment (ISCE): An Earth Science SAR Processing Framework, Toolbox, and Foundry. In: AGU Fall Meeting Abstracts.
- Ahmed, I., 2009. Structural, Stratigraphy, Seismotectonics and Seismic Geohazard Microzonation of New Mirpur, Chatter Pari, Kangra and Thatti Gujran Areas of Districts New Mirpur and Jhelum. University of Azad Jammu and Kashmir, Muzaffarabad, Pakistan, Pakistan.
- Amey, R.M.J., Hooper, A., Walters, R.J., 2018. A Bayesian method for incorporating self-similarity into earthquake slip inversions. *J. Geophys. Res. Solid Earth* 123, 6052–6071.
- Avouac, J.P., Ayoub, F., Leprince, S., Konca, O., Helmberger, D.V., 2006. The 2005, $M_w 7.6$ Kashmir earthquake: Sub-pixel correlation of ASTER images and seismic waveforms analysis. *Earth Planet. Sci. Lett.* 249, 514–528.
- Babur, M., Babel, M.S., Shrestha, S., Kawasaki, A., Tripathi, N.K., 2016. Assessment of climate change impact on reservoir inflows using multi climate-models under RCPs—The case of Mangla Dam in Pakistan. *Water* 8, 389.
- Bassin, C., Laske, G., Masters, G., 2000. The Current Limits of Resolution for Surface Wave Tomography in North America. *EOS Trans. AGU*. 81.
- Biot, M.A., 1941. The general three-dimensional consolidation theory. *J. Appl. Phys.* 12, 155–164.
- Brown, R.L., 1974. Seismic activity following impounding of Mangla Reservoir. *Eng. Geol.* 8, 79–93.
- Chang, K., Chi, W.C., Chen, R.F., Rau, R.J., 2018. Load-induced seismicity near Tsaojing, Taiwan. *Phys. Earth Planet. Inter.* 282, 21–24.
- Chen, C.W., Zebker, H.A., 2002. Phase unwrapping for large SAR interferograms: Statistical segmentation and generalized network models. *IEEE Trans. Geosci. Remote Sens.* 40, 1709–1719.
- Chen, L., Khan, S.D., 2010. InSAR observation of the strike-slip faults in the northwest Himalayan frontal thrust system. *Geosphere* 6, 731–736.
- Davis, D.M., Engelder, T., 1985. The role of salt in fold-and-thrust belts. *Tectonophysics* 119, 67–88.
- Duputel, Z., Vergne, J., Rivera, L., Wittlinger, G., Farra, V., Hetényi, G., 2016. The 2015 Gorkha earthquake: a large event illuminating the Main Himalayan Thrust fault. *Geophys. Res. Lett.* 43, 2517–2525.
- Elliott, J.R., Jolivet, R., González, P.J., Avouac, J.P., Hollingsworth, J., Searle, M.P., Stevens, V.L., 2016. Himalayan megathrust geometry and relation to topography revealed by the Gorkha earthquake. *Nat. Geosci.* 9, 174–180.
- Farr, T.G., Rosen, P.A., Caro, E., Crippen, R., Duren, R., Hensley, S., Seal, D., 2007. The shuttle radar topography mission. *Rev. Geophys.* 45, RG2004.
- Fattahai, H., Agram, P., Simons, M., 2016. A network-based enhanced spectral diversity approach for TOPS time-series analysis. *IEEE Trans. Geosci. Remote Sens.* 55, 777–786.
- Feng, W., Lindsey, E., Barbot, S., Samsonov, S., Dai, K., Li, P., Xu, X., 2017. Source characteristics of the 2015 MW 7.8 Gorkha (Nepal) earthquake and its MW 7.2 aftershock from space geodesy. *Tectonophysics* 712, 747–758.
- Fu, Yuning, Freymueller, Jeffrey T., 2012. Seasonal and long-term vertical deformation in the Nepal Himalaya constrained by GPS and GRACE measurements. *J. Geophys. Res.: Solid Earth* 117.
- Gahalaut, K., Hassoup, A., 2012. Role of fluids in the earthquake occurrence around Aswan reservoir, Egypt. *J. Geophys. Res.: Solid Earth* 117, B02303.
- Gahalaut, K., Gupta, S., Gahalaut, V.K., Mahesh, P., 2018. Influence of tehri reservoir impoundment on local seismicity of northwest Himalaya. *Bull. Seismol. Soc. Am.* 108, 3119–3125.
- Gavillot, Y., Meigs, A., Yule, D., Heermance, R., Rittenour, T., Madugo, C., Malik, M., 2016. Shortening rate and Holocene surface rupture on the Riasi fault system in the Kashmir Himalaya: active thrusting within the Northwest Himalayan orogenic wedge. *Bulletin*. 128, 1070–1094.
- Khani, H., Zeilinger, G., Sobel, E.R., Heidarzadeh, G., 2018. Structural variation within the Himalayan fold and thrust belt: A case study from the Kohat-Potwar Fold Thrust Belt of Pakistan. *J. Struct. Geol.* 116, 34–46.
- Goldstein, R.M., Werner, C.L., 1998. Radar interferogram filtering for geophysical applications. *Geophys. Res. Lett.* 25, 4035–4038.
- González, P.J., Tiampo, K.F., Palano, M., Cannavó, F., Fernández, J., 2012. The 2011 Lorca earthquake slip distribution controlled by groundwater crustal unloading. *Nat. Geosci.* 5 (11), 821–825.
- Gupta, H.K., Rajendran, K., 1986. Large artificial water reservoirs in the vicinity of the Himalayan foothills and reservoir-induced seismicity. *Bull. Seismol. Soc. Am.* 76, 205–215.
- Gupta, H.K., 1985. The present status of reservoir induced seismicity investigations with special emphasis on Koyana earthquakes. *Tectonophysics* 118, 257–279.
- Hainzl, S., Aggarwal, S.K., Khan, P.K., Rastogi, B.K., 2014. Monsoon-induced earthquake activity in Talala, Gujarat, India. *Geophys. J. Int.* 200, 627–637.
- Hainzl, S., Kraft, T., Wassermann, J., Igel, H., Schmedes, E., 2006. Evidence for rainfall-triggered earthquake activity. *Geophys. Res. Lett.* 33, L19303.
- Hsu, Y.J., Kao, H., Bürgmann, R., Lee, Y.T., Huang, H.H., Hsu, Y.F., Zhuang, J., 2021. Synchronized and asynchronous modulation of seismicity by hydrological loading: A case study in Taiwan. *Sci. Adv.* 7 (16), eabf7282.
- Hu, X., Bürgmann, R., 2020. Aquifer deformation and active faulting in Salt Lake Valley, Utah, USA. *Earth Planet. Sci. Lett.* 547, 116471.
- Huang, X., Zhou, T., Turner, A., Dai, A., Chen, X., Clark, R., Wu, B., 2020. The Recent Decline and Recovery of Indian Summer Monsoon Rainfall: Relative Roles of External Forcing and Internal Variability. *J. Clim.* 33, 5035–5060.
- Hussain, A., Yeats, R.S., 2009. Geological setting of the 8 October 2005 Kashmir earthquake. *J. Seismol.* 13, 315–325.

- Iqbal, T., Khan, K., Qaisar, M., Mahmood, T., Ahmad, N., 2009. Mangla Earthquake of March 10, 2006: Source Parameters and Nature of the Derived Fault. *Earthquake* 117–122.
- Jade, S., Shrungeshwara, T.S., Kumar, K., Choudhury, P., Dumka, R.K., Bhu, H., 2017. India plate angular velocity and contemporary deformation rates from continuous GPS measurements from 1996 to 2015. *Sci. Rep.* 7, 1–16.
- Jaeger, J.C., Cook, N.G., 2009. Fundamentals of rock mechanics, fourth ed. Methuen & Co., Ltd., London, p. 513.
- Johnson, C.W., Fu, Y., Bürgmann, R., 2017. Seasonal water storage, stress modulation, and California seismicity. *Science* 356, 1161–1164.
- Jónsson, S., Zebker, H., Segall, P., Amelung, F., 2002. Fault slip distribution of the 1999 M w 7.1 Hector Mine, California, earthquake, estimated from satellite radar and GPS measurements. *Bull. Seismol. Soc. Am.* 92, 1377–1389.
- Kalpana, Chander, R., 2000. Green's function based stress diffusion solutions in the porous elastic half space for time varying finite reservoir loads. *Phys. Earth Planetary Interiors.* 120, 93–101.
- Kayani, S.A., 2013. Mangla Dam Raising: A Review. *Sci. Technolo. Dev.* 32, 149–153.
- Kropáček, J., Braun, A., Kang, S., Feng, C., Ye, Q., Hochschild, V., 2012. Analysis of lake level changes in Nam Co in central Tibet utilizing synergistic satellite altimetry and optical imagery. *Int. J. Appl. Earth Obs. Geoinf.* 17, 3–11.
- Li, Y., Gao, H., Jasinski, M.F., Zhang, S., Stoll, J.D., 2019. Deriving high-resolution reservoir bathymetry from ICESat-2 prototype photon-counting lidar and Landsat imagery. *IEEE Trans. Geosci. Remote Sens.* 57, 7883–7893.
- Madson, A., Sheng, Y., 2020. Reservoir Induced Deformation Analysis for Several Filling and Operational Scenarios at the Grand Ethiopian Renaissance Dam Impoundment. *Remote Sens.* 12, 1886.
- Maussion, F., Schlump, T., & Rothenberg, D. (2020). Salem (Version 0.3). <https://doi.org/10.5281/zenodo.1295582> (accessed 1 March 2021).
- McDougal, J.W., Hussain, A., 1991. Fold and thrust propagation in the western Himalaya based on a balanced cross section of the Surghar Range and Kohat Plateau. *Pakistan AAPG bulletin.* 75, 463–478.
- Oestreicher, N. (2018). Geodetic, hydrologic and seismological signals associated with precipitation and infiltration in the central Southern Alps, New Zealand. (Ph.D. thesis).
- Otsu, N.A., 1979. threshold selection method from gray-level histograms. *IEEE Trans. Syst., Man, Cybern.* 9, 62–66.
- Paul, H., Priestley, K., Powali, D., Sharma, S., Mitra, S., Wanchoo, S., 2018. Signatures of the existence of frontal and lateral ramp structures near the Kishtwar Window of the Jammu and Kashmir Himalaya: evidence from microseismicity and source mechanisms. *Geochem. Geophys. Geosyst.* 19, 3097–3114.
- Pennock, E.S., Lillie, R.J., Zaman, A.S.H., Yousaf, M., 1989. Structural interpretation of seismic reflection data from eastern Salt Range and Potwar Plateau, Pakistan. *AAPG Bull.* 73, 841–857.
- Ramasamy, S.M., Gunasekaran, S., Rajagopal, N., Saravanavel, J., Kumanan, C.J., 2019. Flood 2018 and the status of reservoir-induced seismicity in Kerala, India. *Nat. Hazards.* 99, 307–319.
- Reasenberg, P., 1985. Second-order moment of central California seismicity, 1969–1982. *J. Geophys. Res. Solid Earth* 90 (B7), 5479–5495.
- Rehman, S., Shah, A.N., Mughal, H.U., Javed, M.T., Akram, M., Chilton, S., Nimmo, W., 2016. Geology and combustion perspectives of Pakistani coals from Salt Range and Trans Indus Range. *Int. J. Coal Geol.* 168, 202–213.
- Robert, X., Van Der Beek, P., Braun, J., Perry, C., Dubille, M., Mugnier, J.L., 2009. Assessing Quaternary reactivation of the Main Central thrust zone (central Nepal Himalaya): New thermochronologic data and numerical modeling. *Geology* 37, 731–734.
- Roeloffs, E.A., 1988. Fault stability changes induced beneath a reservoir with cyclic variations in water level. *J. Geophys. Res. Solid Earth* 93, 2107–2124.
- Salman, M., 2019. NMA Situation report No.11 - Mirpur Earthquake 2019, National Disaster Management of Authority. Islamabad. (accessed 1 March 2021) <https://reliefweb.int/sites/reliefweb.int/files/resources/NDMA%20Situation%20Report%20No.%2011%20-%20Mirpur%20Earthquake%202019.pdf>.
- Satyabala, S.P., Yang, Z., Bilham, R., 2012. Stick-slip advance of the Kohat Plateau in Pakistan. *Nat. Geosci.* 5, 147–150.
- Shah, A.A., Abd Manan, N., Aliudin, A., Cahyaningsih, C., Batmanathan, M., Malik, J., 2020. Formation, rotation, and present-day configuration of Kashmir and Peshawar basins in NW Himalaya. *Front. Earth Sci.* 8, 441.
- Sharma, V., Wadhawan, M., Rana, N., Sreejith, K.M., Agrawal, R., Kamra, C., Gahalaut, V.K., 2020. A long duration non-volcanic earthquake sequence in the stable continental region of India: The Palghar swarm. *Tectonophysics* 779, 228376.
- Shi, Y.L., Cheng, H.H., Zhang, B., Zheng, L., Sun, Y.J., Zhang, H., 2013. Are reservoir earthquakes man-made? *WIT Trans. Ecol. Environ.* 178, 273–284.
- Sibson, R.H., 2012. Reverse fault rupturing: competition between non-optimal and optimal fault orientations. *Geological Soc., London, Special Publications* 367, 39–50.
- Simpson, D.W., 1986. Triggered earthquakes. *Annu. Rev. Earth Planet. Sci.* 14, 21–42.
- Steer, P., Simoes, M., Cattin, R., Shyu, J.B.H., 2014. Erosion influences the seismicity of active thrust faults. *Nat. Commun.* 5, 5564.
- Talwani, P., 1997. On the nature of reservoir-induced seismicity. *Pure Appl. Geophys.* 150, 473–492.
- Thakur, V.C., Jayangondaperumal, R., Malik, M.A., 2010. Redefining Medlicott–Wadia's main boundary fault from Jhelum to Yamuna: An active fault strand of the main boundary thrust in northwest Himalaya. *Tectonophysics* 489, 29–42.
- Treloar, P.J., Coward, M.P., 1991. Indian Plate motion and shape: constraints on the geometry of the Himalayan orogen. *Tectonophysics* 191, 189–198.
- Tseng, K.H., Shum, C.K., Kim, J.W., Wang, X., Zhu, K., Cheng, X., 2016. Integrating Landsat Imagers and Digital Elevation Models to Infer Water Level Change in Hoover Dam. *IEEE J. Sel. Top. Appl. Earth Obs. Remote Sens.* 9, 1696–1709.
- Tuan, T.A., Purnachandra Rao, N., Gahalaut, K., Trong, C.D., Van Dung, L., Chien, C., Mallika, K., 2017. Evidence that earthquakes have been triggered by reservoir in the Song Tranh 2 region, Vietnam. *J. Seismol.* 21, 1131–1143.
- Vasyura-Bathke, H., Dettmer, J., Steinberg, A., Heimann, S., Isken, M.P., Zielke, O., Jónsson, S., 2020. The Bayesian Earthquake Analysis Tool. *Seismol. Res. Lett.* 91, 1003–1018.
- Wang, H., Liu-Zeng, J., Ng, A.M., Ge, L., Javed, F., Long, F., Shao, Z., 2017. Sentinel-1 observations of the 2016 Menyuan earthquake: A buried reverse event linked to the left-lateral Haiyuan fault. *Int. J. Appl. Earth Obs. Geoinf.* 61, 14–21.
- Wessel, P., Luis, J.F., Uieda, L., Scharroo, R., Wobbe, F., Smith, W.H.F., Tian, D., 2019. The generic mapping tools version 6. *Geochem. Geophys. Geosyst.* 20, 5556–5564.
- Xu, H., 2006. Modification of normalised difference water index (NDWI) to enhance open water features in remotely sensed imagery. *Int. J. Remote Sens.* 27, 3025–3033.
- Xu, W., Bürgmann, R., Li, Z., 2016. An improved geodetic source model for the 1999 Mw 6.3 Chamoli earthquake, India. *Geophys. J. Int.* 205, 236–242.
- Zhai, G., Shirzaei, M., Manga, M., Chen, X., 2019. Pore-pressure diffusion, enhanced by poroelastic stresses, controls induced seismicity in Oklahoma. *PNAS* 116, 16228–16233.